Chinese Chemical Letters 37 (2026) 112025

Contents lists available at ScienceDirect

Chinese Chemical Letters

journal homepage: www.elsevier.com/locate/cclet

Hybrid lignin-intercalated MXene membranes for enhanced osmotic energy conversion

Xing Zhang[a], Yumei Wang[a], Yuntao Zhao[b], Yue Sun[a,*], Yasong Chen[c,*], Lei Nie[d,*], Zhenglong Li[e,*]

[a] State Key Laboratory of Advanced Separation Membrane Materials, School of Chemistry, School of Materials Science and Engineering, Tiangong University, Tianjin 300387, China
[b] School of Materials and Chemical Engineering, Ningbo University of Technology, Ningbo 315211, China
[c] National Engineering Research Center of Eco-environment Protection for Yangtze River Economic Belt, China Three Gorges Corporation, Wuhan 430012, China
[d] National Key Laboratory of Biobased Transportation Fuel Technology, Department of Polymer Science and Engineering, Zhejiang University, Hangzhou 310058, China
[e] National Key Laboratory of Biobased Transportation Fuel Technology, College of Biosystems Engineering and Food Science, Zhejiang University, Hangzhou 310058, China

ARTICLE INFO

Article history:
Received 28 May 2025
Revised 22 August 2025
Accepted 26 October 2025
Available online 28 October 2025

Keywords:
2D-membrane
MXene
Lignin
Lamellar architecture
Reverse electrodialysis

ABSTRACT

Two-dimensional (2D) materials exhibit great potential for osmotic power generation due to their high membrane selectivity. However, performance enhancement remains hindered by substantial resistance arising from tortuous ion transport pathways within 2D nanofluidic membranes. MXenes, a novel class of 2D layered materials, have garnered significant attention as promising candidates for reverse electrodialysis (RED) membranes due to their laminated nanochannels and surface-charged functional groups. Although MXene-derived ion-exchange membranes display exceptional ionic discrimination capabilities and enhanced charge transport properties, their implementation in practical systems is limited by structural fragility and compromised performance under hydrated conditions, primarily due to weak interlayer interactions, restricting their RED performance. This study demonstrates an MXene-sodium ligninsulfonate (MSL) lamellar architecture to feature record-low internal resistance, achieving breakthrough osmotic energy conversion efficiency through synergistic interfacial engineering. In addition, the well-aligned MXene framework significantly shortens ion permeation pathways, thus lowering internal resistance. As a result, the MSL membrane delivers a high power density of approximately 22.15 W/m^2 when mixing artificial seawater and river water, representing a 6.78-fold improvement over pristine MXene membranes. This interfacial engineering protocol addresses the longstanding trade-off between ion selectivity and membrane durability in nanofluidic systems, paving the way for the practical implementation of MXene-based technologies in marine energy conversion.

© 2026 Published by Elsevier B.V. on behalf of Chinese Chemical Society and Institute of Materia Medica, Chinese Academy of Medical Sciences.

Amid global commitments to carbon neutrality and the urgent need to eliminate the $5.3 trillion annual fossil fuel subsidies, the scientific community is accelerating the development of marine energy harvesters capable of generating continuous power from salinity gradients, a clean energy reservoir [1]. Osmotic energy, commonly referred to as blue energy, derived from salinity gradients, represents a renewable and clean energy source. Efficient capture and conversion of this energy can help alleviate global energy shortages [2]. Reverse electrodialysis (RED), a membrane-based technology, has demonstrated considerable promise for harvesting salinity gradient energy from seawater and river water interfaces [3]. Central to the RED process is the ion-exchange membrane, which plays a pivotal role in determining system performance. Current limitations in osmotic power generation are primarily attributed to the structural-property mismatches in commercially available ion-selective membranes. As demonstrated in recent studies [4,5], the densely packed polymer networks and nanoconfined channels that characterize of conventional cation-exchange membranes inevitably lead to three critical challenges: (i) An exponentially increasing transmembrane resistance under high salinity gradients, (ii) degraded charge selectivity due to Debye

* Corresponding authors.
E-mail addresses: sunyue@tiangong.edu.cn (Y. Sun), chen_yasong@ctg.com.cn (Y. Chen), leinie@zju.edu.cn (L. Nie), zhenglongli@zju.edu.cn (Z. Li).

https://doi.org/10.1016/j.cclet.2025.112025
1001-8417/© 2026 Published by Elsevier B.V. on behalf of Chinese Chemical Society and Institute of Materia Medica, Chinese Academy of Medical Sciences.

screening effects, and (iii) irreversible performance decay caused by swelling-induced pore collapse.

Substantial research efforts have been directed toward improving membrane properties, specifically mechanical strength, operational lifespan, and spatial charge distribution, to extend usage duration and optimize localized charge behavior to raise the industrial application of RED. In recent years, two-dimensional (2D) nanofluidic membrane assemblies have received increasing attention for osmotic energy harvesting due to their precise control over ion transport at the nanoscale [6]. The well-defined channel spacing and ordered interlayer architectures of 2D materials make them highly promising for facilitating ion flow, energy conversion, and ions separating based on size or charge. Materials such as graphene oxide, boron nitride, clays, metal–organic frameworks (MOFs), and covalent organic frameworks (COFs) have exhibited good ion discrimination, directional ion transport, and controllable gating properties, presenting new opportunities for developing of RED membranes [7–12]. Nonetheless, these materials face challenges, including high production costs, complex synthesis procedures, and low surface charge densities.

MXenes-emerging 2D transition metal carbides/nitrides with surface-terminated polar moieties (•F, •OH, •O), exhibit outstanding aqueous processability and tunable surface charge properties (Figs. S1 and S2 in Supporting information), making them ideal building blocks for constructing nanofluidic architectures [13]. Although these stacked nanosheet assemblies display promising ion transport dynamics and osmotic energy conversion potential [14], their practical application remains limited by structural vulnerabilities caused by weak interlayer adhesion energies and hydration-induced layer expansion, which severely restrict their assembly and deployment without adhesives. Lignin, the second most abundant biopolymer on Earth, consists of a three-dimensional aromatic network of phenylpropane units and is rich in hydroxyl groups and ether linkages [15–17]. As a structural component of lignocellulosic biomass, lignin naturally supports the transport of water and nutrients and exhibits a strong affinity for water molecules [18]. Sulfonated lignin (SL), a chemically modified variant containing numerous sulfonic acid groups, has been widely utilized in proton conduction technologies due to its high hydrophilicity and proton-conducting functional groups. SL is a renewable derivative of lignin, with abundant availability and low associated cost. SL contains abundant sulfonic acid groups and aromatic ring structures, which have the capacity to form strong interactions with the MXene surface [19].

This study uses SL as a multifunctional intercalator within MXene interlayers to fabricate highly conductive MXene-SL membranes. The sulfonic acid groups and ether linkages in SL serve as proton donors and acceptors, respectively, introducing additional proton-hopping sites and establishing a continuous hydrogen-bond network within the MXene nanochannels. The synergistic interaction of these functional groups effectively lowers the energy barrier for proton transport, substantially enhancing the proton conductivity of MXene-SL membranes. The customized reservoir is shown in Fig. S3 (Supporting information). The MSL membrane achieves a high-power density of approximately 22.15 W/m^2 when mixing artificial seawater and river water, representing a 6.78-fold improvement compared to pristine MXene membranes.

Sulfonated lignin, a sulfonation-modified derivative of lignin, contains abundant sulfonic acid groups that regulate surface chemical interactions and prevent excessive restacking of MXene nanosheets [20,21]. A detailed characterization of SL is presented in Fig. S4 (Supporting information). The preparation process of the MXene-SL composite membrane is illustrated in Figs. 1a and b. Fig. 1c is a real picture of MSL membrane. Due to the good dispersion stability and compact stacking of nanosheets in solution, the vacuum-filtered membrane displays a highly dense structure, the mechanical properties have also improved (Fig. S5 in Supporting information), with no visible delamination observed in SEM images (Fig. 1d, Figs. S6 and S7 in Supporting information) a layered structure similar to that found in biological models is evident. Fig. 1e is a schematic diagram of the MSL composite membrane structure and separation mechanism. The incorporation of SL not only enhances the interlayer bonding between MXene sheets but also promotes the development of uniform, defect-free composite membranes (Fig. S8 in Supporting information).

Cross-sectional SEM images reveal a well-defined layered structure that enables rapid ion transport. In addition, SL molecules are distinctly intercalated between MXene layers, causing changes in interlayer spacing. This observation is further validated by small-angle XRD analysis (Fig. 2a). The interlayer spacing of pristine MXene, calculated using the Bragg equation [22], measures 1.39 nm. After SL intercalation, the spacing expands to 1.55, 1.66, and 1.68 nm for MXene-to-SL mass ratios of 1:1, 1:2, and 1:3, respectively. This expansion introduces additional ion transport pathways and confirms the successful integration of SL into the MXene framework.

The bonding mechanism between SL and MXene is further investigated using X-ray photoelectron spectroscopy (XPS) (Figs. 2b and c, Fig. S9 in Supporting information). Distinct changes are observed in the C 1s spectra. Deconvolution of the C 1s spectrum for pristine MXene reveals four characteristic peaks at 282.03, 284.71, 286.11, and 288.62 eV, corresponding to C–C, C–O, C = O, and O–C = O groups, respectively. In the MXene-SL composite membrane, the C 1s spectrum exhibits peaks at 282.03, 284.69, 286.12, and 288.67 eV, assigned to the same groups [23,24]. The shift in C–O stretching vibration, along with the C = O bond shift in FTIR spectra, quantitatively confirms the reconstruction of interfacial hydrogen bonding. Additional data from FTIR spectroscopy further support the successful modification of MXene by SL (Fig. S10 in Supporting information).

For practical use, membrane materials must demonstrate sufficient water stability. Pristine MXene membranes undergo severe structural degradation after only 5 min of ultrasonic treatment in water, whereas MXene-SL composite membranes display good stability (Fig. 2d). Brunauer-Emmett-Teller (BET) analysis identifies a pore size distribution of approximately 2.7 nm for the MSL layer (Fig. 2e). The SL modification also improve the surface charge density of the nanosheets (Fig. 2f). Water resistance is additionally assessed using static water contact angle measurements (Fig. S11 in Supporting information). The contact angle of the MSL2 composite membrane is 47.33°, reflecting its hydrophilic character and improved aqueous stability. SL functions as an interlocking agent, strengthening the MXene nanosheets through robust hydrogen bonding (Fig. 1e). The active groups on the benzene ring and side chains in the structure of lignin sulfonate, such as hydroxyl, carboxyl and sulfonic acid groups, serve as binding sites for complexation with metal ions, forming lignin metal ion chelates.

An MXene-SL composite membrane is placed mounted between two custom-designed electrochemical testing chambers to assess the ion transport behavior (Fig. 3a). Transmembrane ion diffusion characteristics are evaluated by recording current–voltage (*I-V*) curves. Potassium chloride (KCl) is selected as the probe electrolyte due to the similar ionic mobilities and radii of K^+ and Cl^-. Fig. 3b indicates that the *I-V* curves of the MXene-SL composite membrane in KCl electrolyte exhibit linear Ohmic behavior with minimal ion current rectification, indicating the presence of continuous, electrically conductive pathways and a structurally symmetric membrane [8]. Ion conductance, derived from the *I-V* curves (Fig. 3c), reveals two distinct regimes. At high KCl concentrations (>0.01 mol/L), ion conductance demonstrates a linear correlation with concentration, reflecting bulk transport behavior. In contrast, at low KCl concentrations (<0.01 mol/L), the conductance levels off,

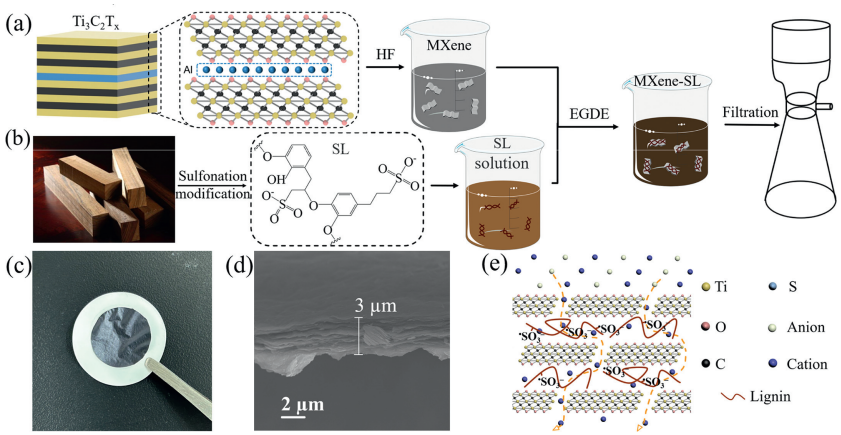


Fig. 1. Design and structural characterization of MSL composite membranes. (a, b) Schematic diagrams illustrating the preparation process of MSL composite membranes. (c) Digital photograph of an MSL composite membrane. (d) SEM images of the MSL composite membranes. (e) Schematic diagram of the structure and separation mechanism of MSL composite membrane.

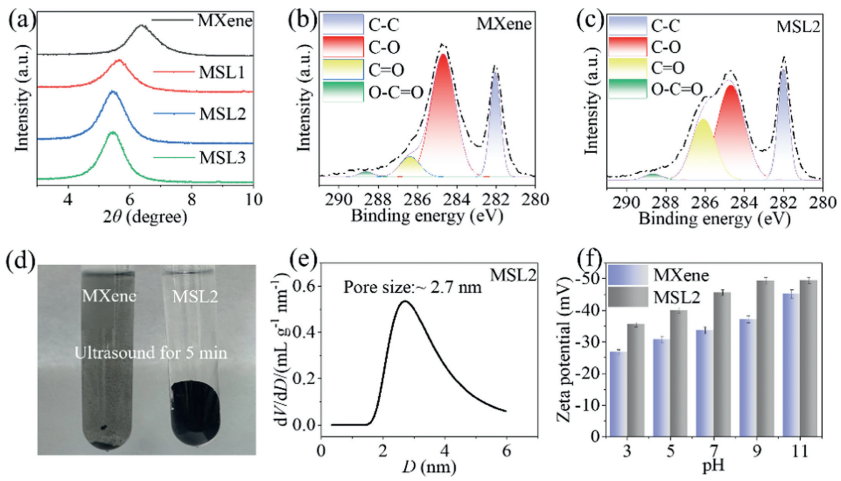


Fig. 2. Structural and surface characterization of MSL composite membranes. (a) Low-angle XRD spectra of the composite membrane. (b) C 1s XPS spectrum of the MXene membrane. (c) C 1s XPS spectrum of the MSL membranes. (d) Water stability of MXene and MSL membranes. (e) Pore size distribution of the heterogeneous membrane. (f) Zeta potential of the MXene dispersion.

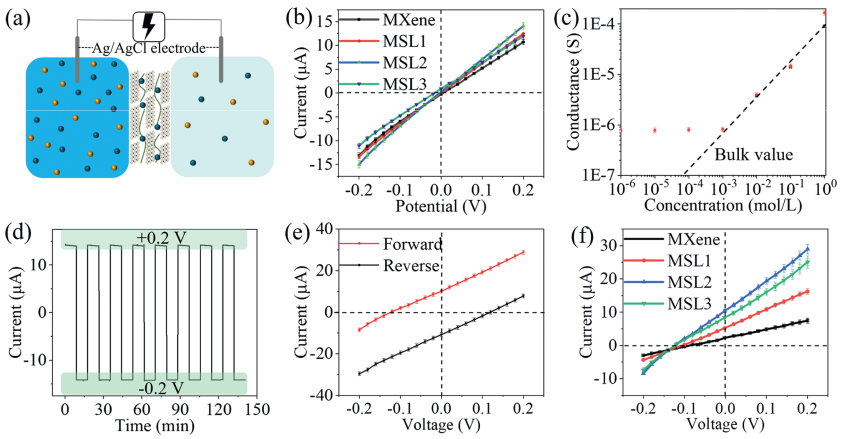


Fig. 3. (a) Cross-sectional schematic of the nanofluidic testing platform employing symmetric Ag/AgCl electrodes. (b) Linear current-voltage responses demonstrate Ohmic behavior across KCl. (c) Surface-charge-governed ion transport is evidenced by the linear conductance-concentration relationship, deviating markedly from bulk solution behavior below 0.01 mol/L KCl. (d) The *I-T* response of the MSL membrane was measured in 0.01 mol/L KCl with an applied alternating ± 0.2 V bias. (e) *I-V* curves of the MSL membrane under a 50-fold NaCl concentration gradient in both forward and reverse diffusion directions to evaluate ion transport stability. (f) *I-V* curves of the MSL membrane measured under a 50-fold NaCl concentration gradient.

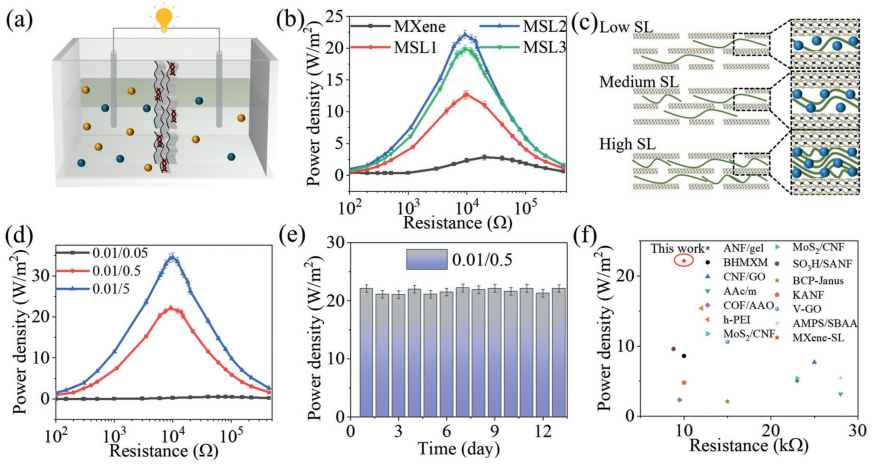


Fig. 4. (a) Diagram illustrating the mechanism of energy conversion driven by a salinity gradient. (b) Influence of sodium ligninsulfonate concentration on the output power density. (c) Conceptual diagram showing the role of SL content in modulating the energy conversion behavior. (d) Variation in output power density of the MSL2 membrane with increasing external resistance under 5×, 50×, and 500× salinity gradient conditions. (e) Assessment of the long-term operational stability of the SL-based composite membrane in simulated seawater and river water environments. (f) The osmotic energy harvesting performance was then compared with that of previously reported membrane-based systems under a 50-fold concentration gradient.

indicating that surface charge effects govern ion transport within the confined nanochannels [25].

The ion transport stability of the MXene-SL membrane was further evaluated using alternating current (AC) measurements. A sinusoidal voltage of ±0.2 V was applied, and the current-time (*I-T*) response was recorded (Fig. 3d). Each cycle lasted 16 min, and a total of eight continuous cycles were conducted. The symmetric and stable positive and negative current responses confirm the high ion transport stability achieved by the composite membrane. Current–voltage (*I-V*) curves were obtained under salt concentration gradients to clarify the ion transport mechanism. Due to the cation-selective nature of the membrane, K^+ preferentially diffused from the high- to the low-concentration side, resulting in both a diffusion current and a diffusion potential [26]. In this experiment, the NaCl concentration on the low-concentration side was fixed at 0.01 mol/L, with a 50-fold concentration gradient. Commercial Ag/AgCl electrodes (Lei-ci 208) were utilized to eliminate interfacial potential discrepancies commonly associated with self-fabricated electrodes under different ionic strengths. The measured diffusion parameters under these conditions reflected the I_{SC} and V_{OC}, as derived from the *I-V* curves. Fig. 3e indicates that the *I-V* curves of the MXene-SL (1:2) membrane under forward and reversed 50-fold concentration gradients (0.01/0.5 mol/L NaCl) exhibited nearly identical profiles, confirming the symmetric structure of the composite membrane and the absence of a preferred ion diffusion direction. The *I-V* curves under these conditions (Fig. 3f) indicate that the optimal energy conversion performance was achieved at an MXene-to-SL ratio of 1:2. The corresponding cation transference numbers (τ_n) were 0.74, 0.63, and 0.57, with associated energy conversion efficiencies (η) of 11.33 %, 3.43 %, and 0.95 %, respectively (Fig. S12 and Table S1 in Supporting information) [27–29].

Salinity gradient energy conversion tests were conducted using synthetic seawater (0.5 mol/L NaCl) and simulated river water (0.01 mol/L NaCl) as representative high- and low-salinity sources to evaluate the practical applicability of the membranes nanofluidic system (Fig. 4a). The power density generated by the composite membranes was measured under different sulfonated lignin contents, with MXene-to-SL mass ratios of 1:1, 1:2, and 1:3 to enhance performance (Fig. 4b and Fig. S13 in Supporting information). The corresponding maximum output power densities reach 12.71, 22.15, and 19.89 W/m^2, respectively. The output power density initially rises with increasing SL content, reaching its peak at the 1:2 ratio. The MSL membrane is negatively charged, which attracts $^{\bullet}Na^+$ and accelerates its transport, enabling the conversion of osmotic energy. Lignin contains $^{\bullet}SO_3^-$ groups that interact with $^{\bullet}Na^+$ and further enhance membrane performance. However, an additional increase in SL content led to decreased performance, attributed to excessive SL partially blocking the two-dimensional nanochannels and introducing additional physical resistance. This effect ion transport, lowers ion flux, and ultimately reduces power output (Fig. 4c) [7,27].

In addition, energy conversion performance was assessed under 5-fold and 500-fold salinity gradients, yielding output power densities of 0.51 and 34.54 W/m^2, respectively (Fig. 4d). Long-term stability and durability, critical for practical-applications, were investigated over 13 days under sustained artificial seawater river water gradients. Fig. 4e shows that the MXene-SL (1:2) composite membrane maintained an output power density of 22.15 W/m^2, with only a 4.3 % decrease from the initial value, demonstrating good operational stability. The composite membrane also demonstrated good hydrolytic stability (Fig. S14 in Supporting information). This strong performance is attributed to the chemical stability of the MXene-SL composite and the robust hydrogen-bonding interlock between MXene nanosheets and SL molecules. The power density achieved by this heterogeneous membrane significantly exceeds that of most nanofluidic membranes previously reported for salinity gradient energy harvesting (Fig. 4f) [30–41].

This study develops a high-performance MXene-sulfonated lignin (MXene-SL) composite membrane for efficient nanofluidic osmotic energy harvesting. The incorporation of sulfonated lignin significantly improves the water stability of MXene membranes by enhancing interlayer binding through strong hydrogen bonding interactions. The SL content plays a pivotal role in optimizing salinity gradient energy conversion efficiency. The active groups on the benzene ring and side chains in the SL structure, such as hydroxyl, carboxyl, and sulfonic acid groups, can act as sites for complexing with metal ions (Na^+, K^+, and others), forming lignin-metal ion chelates and enhancing the selective transport of cations. Although increasing the SL content expands the interlayer spacing and enhances ion flux, excessive SL disrupts ion transport channels, introduces additional internal resistance, and results in performance degradation. Under osmotic-driven conditions, with a 50-fold salinity gradient (0.01 mol/L NaCl as artificial river water and 0.5 mol/L

NaCl as seawater), the composite membrane delivers a remarkable output power density of 22.15 W/m^2. The power density decreases by only 4.3 % after 13 days, indicating good long-term reliability and sustained functionality. The low-cost construction of this composite membrane presents a promising strategy for efficiently harnessing salinity gradient energy, providing a sustainable alternative power source [42].

Declaration of competing interest

The authors declare that they have no known competing financial interests or personal relationships that could have appeared to influence the work reported in this paper.

CRediT authorship contribution statement

Xing Zhang: Writing – original draft, Methodology. **Yumei Wang:** Visualization, Investigation. **Yuntao Zhao:** Investigation, Formal analysis. **Yue Sun:** Writing – review & editing, Supervision. **Yasong Chen:** Writing – review & editing, Supervision. **Lei Nie:** Writing – review & editing, Supervision. **Zhenglong Li:** Writing – review & editing, Supervision.

Acknowledgments

The authors gratefully acknowledge the research funding provided by National Natural Science Foundation of China (Nos. 22473086, 22478339), the Distinguished Natural Scientific Foundation of Tianjin (No. 24JCJQJC00100), General Programs of the Natural Science Foundation of Xinjiang (No. 2025DA072) and Hebei Natural Science Foundation (No. B2024110030).

Supplementary materials

Supplementary material associated with this article can be found, in the online version, at doi:10.1016/j.cclet.2025.112025.

References

[1] Z. Zhang, L. Wen, L. Jiang, Nat. Rev. Mater. 6 (2021) 622–639.
[2] B.E. Logan, M. Elimelech, Nature 488 (2012) 313–319.
[3] S. Hou, Q. Zhang, Z. Zhang, et al., Nano Energy 79 (2021) 105509.
[4] G. Bian, N. Pan, Z. Luan, et al., Angew. Chem. Int. Ed. 60 (2021) 20294–20300.
[5] W. Chen, Y. Xiang, X.Y. Kong, L. Wen, Giant 10 (2022) 100094.
[6] W. Xin, L. Jiang, L. Wen, Acc. Chem. Res. 54 (2021) 4154–4165.
[7] J. Wang, Z. Zhang, J. Zhu, et al., Nat. Commun. 11 (2020) 3540.
[8] K.R. Bang, C. Kwon, H. Lee, S. Kim, E.S. Cho, ACS Nano 17 (2023) 10000–10009.
[9] C. Chen, D. Liu, L. He, et al., Joule 4 (2020) 247–261.
[10] R. Qin, J. Tang, C. Wu, et al., Nano Energy 100 (2022) 107526.
[11] G. Laucirica, J.A. Allegretto, M.F. Wagner, et al., Adv. Mater. 34 (2022) 2207339.
[12] L. Cao, X. Liu, D.B. Shinde, et al., Angew. Chem. Int. Ed. 61 (2021) e202113141.
[13] X. Li, Z. Huang, C.E. Shuck, et al., Nat. Rev. Chem. 6 (2022) 389–404.
[14] H. Qin, H. Wu, S.M. Zeng, et al., Adv. Membr. 2 (2022) 100046.
[15] Y.T. Chen, Y.M. Sun, C.C. Hu, J.Y. Lai, Y.L. Liu, Adv. Membr. 2 (2021) 3099–3106.
[16] P. Figueiredo, K. Lintinen, J.T. Hirvonen, M.A. Kostiainen, H.A. Santos, Prog. Mater Sci. 93 (2018) 233–269.
[17] Y. Ge, D. Xiao, Z. Li, X. Cui, J. Mater. Chem. A 2 (2014) 2136–2145.
[18] J. Zhu, C. Yan, X. Zhang, et al., Prog. Energ. Combust. 76 (2020) 100788.
[19] Q. Wang, X. Pan, C. Lin, et al., Chem. Eng. J. 370 (2019) 1039–1047.
[20] M.J. Tao, S.Q. Cheng, et al., J. Membr. Sci. 662 (2022) 120965.
[21] Y. Liu, X. Mao, H. Wu, et al., J. Membr. Sci. 644 (2022) 120126.
[22] Y.T. Liu, P. Zhang, N. Sun, et al., Adv. Mater. 30 (2018) 1707334.
[23] A. Rozmysłowska-Wojciechowska, T. Wojciechowski, W. Ziemkowska, et al., Appl. Surf. Sci. 473 (2019) 409–418.
[24] C. Ma, W.T. Cao, W. Zhang, et al., Chem. Eng. J. 403 (2021) 126438.
[25] K. Raidongia, J. Huang, J. Am. Chem. Soc. 134 (2012) 16528–16531.
[26] D.K. Kim, C. Duan, Y.F. Chen, A. Majumdar, Microfluid. Nanofluid. 9 (2010) 1215–1224.
[27] L. Ding, M. Zheng, D. Xiao, et al., Angew. Chem. Int. Ed. 61 (2022) e202206152.
[28] Y. Xu, Y. Song, F. Xu, Nano Energy 79 (2021) 105468.
[29] N. Sheng, M. Zhang, Q. Song, et al., Nano Energy 101 (2022) 107548.
[30] Q. Luo, P. Liu, L. Fu, et al., ACS Appl. Mater. Interfaces 14 (2022) 13223–13230.
[31] R. Duan, J. Zhou, X. Ma, et al., Nano Lett. 23 (2023) 11043–11050.
[32] W. Xin, Z. Zhang, X. Huang, et al., Nat. Commun. 10 (2019) 3876.
[33] W. Chen, Q. Zhang, Y. Qian, et al., ACS Cent. Sci. 6 (2020) 2097–2104.
[34] C. Li, L. Wen, X. Sui, et al., Sci. Adv. 7 (2021) eabg2183.
[35] M. Chen, K. Yang, J. Wang, et al., Adv. Funct. Mater. 33 (2023) 2302427.
[36] C. Zhu, P. Liu, B. Niu, et al., J. Am. Chem. Soc. 143 (2021) 1932–1940.
[37] Z. Man, J. Safaei, Z. Zhang, et al., J. Am. Chem. Soc. 143 (2021) 16206–16216.
[38] Z. Zhang, X. Sui, P. Li, et al., J. Am. Chem. Soc. 139 (2017) 8905–8914.
[39] L. Ding, D. Xiao, Z. Zhao, et al., Adv. Sci. 9 (2022) e2202869.
[40] Z. Zhang, W. Shen, L. Lin, et al., Adv. Sci. 7 (2020) 2000286.
[41] K.T. Huang, W.H. Hung, Y.C. Su, et al., Adv. Funct. Mater. 33 (2023) 2211316.
[42] L. Yang, C.Y. Zhang, H.L. Zhang, et al., Chem. Soc. Rev. 54 (2025) 7377–7420.